Journal of Applied Physics

RESEARCH ARTICLE | MARCH 05 2020

An effective Xe^+–Xe interaction potential for electric propulsion systems

Jiahong Wang ; Yazhong Jiang ; Laiwen Chen ; Chun-Hian Lee

J. Appl. Phys. 127, 093302 (2020)
https://doi.org/10.1063/1.5120110

Journal of Applied Physics ARTICLE scitation.org/journal/jap

An effective Xe^+–Xe interaction potential for electric propulsion systems

Cite as: J. Appl. Phys. **127**, 093302 (2020); doi: 10.1063/1.5120110
Submitted: 16 July 2019 · Accepted: 15 February 2020 ·
Published Online: 5 March 2020

Jiahong Wang,[1] Yazhong Jiang,[2] Laiwen Chen,[1,a)] and Chun-Hian Lee[1]

AFFILIATIONS

[1]School of Aeronautic Science and Engineering, Beihang University, Beijing 100083, People's Republic of China
[2]Department of Mechanical Engineering, The Hong Kong Polytechnic University, Kowloon, Hong Kong, People's Republic of China

[a)]**Author to whom correspondence should be addressed:** Lwchen@buaa.edu.cn

ABSTRACT

An effective Xe^+–Xe interaction potential for electric propulsion systems is proposed based on both spin–orbit free interaction potentials and the screened-Coulomb potential. The model not only conforms with the potential obtained by an *ab initio* method at large internuclear distances but also matches well with the potential derived from experimental scattering data at short internuclear distances. The scattering angles and differential cross sections computed by the effective potential are in good agreement with those obtained by the Morse potential in low-energy regions and those via two screened-Coulomb potentials (the Ziegler–Biersack–Littmark and Zinoviev potential) in high-energy regions, respectively. To further validate the effective potential, a particle-in-cell method with a Monte Carlo collisions technique, coupled with a direct method for solving the scattering equation, was applied to simulate the collisions of 1500-eV and 7000-eV single-charged xenon ions with background xenon atoms in a test cell. The simulated currents on the inner cylinder, exit plate, exit orifice, and front plate are calculated by different potentials. Results show that the effective potential can give a good prediction of the Xe^+–Xe elastic collisions in the wider energy region compared with the Morse, Ziegler–Biersack–Littmark, and Zinoviev potentials.

I. INTRODUCTION

Xenon has become the main working medium for electric propulsion due to its low ionization energy and large molecular mass.[1] The elastic collision between Xe^+ (commonly from hundreds to thousands of eV) and Xe (at several hundred K) may generate a momentum exchange (MEX) or charge exchange (CEX) process, either in the thrust chamber or in the plume. Both interacting processes contribute to the transport of energy and momentum between the ion and atom, causing a loss of thrust. In addition, the CEX collision process is characterized by the transmission of an electron between Xe^+ and Xe that may result in the formation of a fast Xe atom and a slow Xe^+ ion. Meanwhile, most of the CEX and a part of the MEX collision can lead to large-angle ion scattering. Influenced by electrostatic fields, these large-angle scattering ions can induce backflow or sputtering on the wall or grids, thus eroding the spacecraft and reducing the lifetime of the electric thruster. An accurate elastic scattering model of Xe^+ and Xe is required to give a reasonable prediction of ion movement and to provide a basic tool for the design of electric propulsion thrusters.

An assumption has been made that there is no momentum or energy exchange between Xe^+ and Xe but only electron transfer in collision processes.[2] Subsequently, the variable hard sphere (VHS) model[3] has been employed to simulate elastic collisions using isotropic scattering in conjunction with conservation of momentum and energy.[4–6] In fact, CEX interaction can be regarded as a subset of elastic collisions. Accordingly, a more detailed model has been developed based on anisotropic scattering and used to predict MEX and CEX collisions in the plume of electric propulsion.[7,8]

In reality, the scattering processes between Xe^+ and Xe are very complicated, especially when taking into account the fine-structure states and the phase interference from coherent pairs.[10–12] Therefore, the interactions between Xe^+ and Xe can show different scattering phenomena. However, relevant studies on the thrust chamber or the plume of electric propulsion are mainly focused on the macroscopic properties of the ions. Accordingly, it is straightforward to simulate the elastic scattering employed in a semi-empirical potential model. This model has been widely used in molecular dynamics and Monte Carlo simulation studies.[13]

To simulate Xe^+–Xe elastic collisions, one can use either the scattering equation directly[9,14] or the relationship between the scattering angle and the differential cross section.[8,15] Whichever method is used, an accurate and simple effective interaction potential model must first be determined. At present, the Morse potential proposed by Chiu *et al.*[16] is a typical Xe^+–Xe interaction model applied in Monte Carlo simulation.[14,15,17,18] This potential is obtained by fitting spin–orbit free potential energy curves.[19] Although in most cases the Morse model is suitable for the computation of elastic collisions, its disadvantage is that it would give a finite value as the internuclear distance approaches zero.[13] More seriously, when the impact parameter equals zero, there is no solution to the trajectory turning point if the relative energy in the center of mass (CM) frame is greater than the maximum value of the potential.

Although the screened-Coulomb potentials[13] can give a good prediction of ion–atom or atom–atom elastic collisions at short internuclear distance,[35–43] almost all of the screened-Coulomb potentials are purely repulsive models without allowing for the attractive effect. In Ref. 18, the purely repulsive potential of the $^2\Sigma_g$ state is employed to calculate the deflection functions and the differential cross sections. The results using this repulsive model are significantly different from those obtained by the Morse function.

For electric propulsion, interest is increasing in both higher specific impulse and longer lifetime for future deep-space scientific missions. In addition, ion source devices based on the ion thruster technology can be utilized to sputter clean, sputter coat, ion plate, and ion implant, which should also take the high-energy ions into consideration.[44,45] Therefore, it is necessary to investigate both low and high energy collisions to further understand the mechanism of the plasma flows.

Regarding this problem, in this study, an effective Xe^+–Xe interaction potential is proposed based on both spin–orbit free interaction potentials and the screened-Coulomb potential. Compared with the Morse,[16] Ziegler–Biersack–Littmark (ZBL),[38] and Zinoviev potentials,[39] the model not only conforms with the interaction potential based on an *ab initio* method[19] in low-energy regions but also matches well with the potential derived from experimental scattering data[42] in high-energy regions. To validate the predictive performance of the model, the particle-in-cell Monte Carlo collisions (PIC-MCC) technique,[20] coupled with a direct method for solving the scattering equation, is employed to simulate collisions between 1500-eV, single-charged xenon ions and background xenon atoms in a test cell, the benchmark problem as performed in Refs. 21 and 22. Comparisons are made among the simulated results together with the potential derived from experimental scattering data[42] to demonstrate the accuracy of the model. Additionally, collisions between 7000-eV Xe^+ and Xe in the test cell are simulated to show the disparities between different models at high energy.

II. THEORETICAL MODEL

A. Interaction potential at large distances

The interaction potentials for Xe^+–Xe collisions at large internuclear distance have been obtained by an *ab initio* method,[19,23]

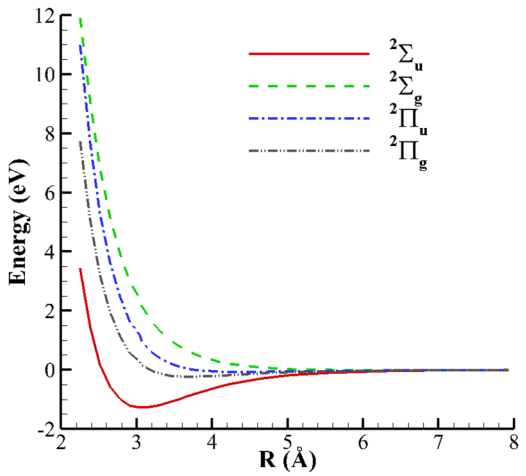

FIG. 1. Spin–orbit free interaction potentials.[19]

presenting four spin–orbit free potentials with $^2\Sigma_u$, $^2\Sigma_g$, $^2\Pi_u$, and $^2\Pi_g$ states. Figure 1 shows the four potential curves calculated by Paidarová and Gadea.[19] The $^2\Sigma_u$ state is balanced with regard to attractive and repulsive behaviors, while the $^2\Pi_g$ and $^2\Pi_u$ states possess a weakly attractive and strongly repulsive character, while the $^2\Sigma_g$ state possesses the strongest repulsive force among the four potentials.

In order to solve problems based on molecular dynamics, an analytical expression for the potential must be provided. The expression can usually be constructed via fitting the numerical data. Amarouche *et al.*[23] and Katz *et al.*[24] used Morse functions coupled with repulsive functions to fit the above four spin–orbit free interaction potential curves. Chiu *et al.*[16] applied Morse functions to fit the Σ and Π pair of the interaction potentials,[19] and the expression can be written as follows:

$$V(R) = D_e[e^{2b_0(r_e-R)} - 2e^{b_0(r_e-R)}], \quad (1)$$

where V is the interaction potential; R is the internuclear distance; and D_e, b_0, and r_e are the model parameters given in Table I. Since there is no unified expression available for the Morse potential based on the four states, one way of furnishing the formalism is to average the two pairs of Morse functions, which gives

$$V_{Morse}(R) = W_\Sigma V_{Morse,\Sigma}(R) + W_\Pi V_{Morse,\Pi}(R), \quad (2)$$

TABLE I. Morse potential parameters for Σ pair and Π pair of the spin–orbit free potentials.[16] W is the statistical weight. Values are given in atomic units.

Potential	W	D_e	b_0	r_e
Σ_{u+g}	1/3	0.005 85	0.645	7.476
Π_{u+g}	2/3	0.004 87	0.677	7.570

where V_{Morse} is the averaged potential in Morse form, W_Σ and W_Π are the statistical weights in the Σ pair and Π pair, respectively, and $V_{Morse,\Sigma}$ and $V_{Morse,\Pi}$ are the Morse potentials in their respective states.

The scattering angle of the CM frame, θ_{CM}, can be obtained if the relative collision energy E_T, the impact parameter b, and the interaction potential $V(R)$ are specified.[25] Accordingly,

$$\theta_{CM}(E_T, b) = \pi - \int_{R_0}^{\infty} \frac{dR}{R^2[1 - b^2/R^2 - V(R)/E_T]^{1/2}}, \quad (3)$$

where R_0 is the trajectory turning point, namely, the minimum distance of approach. Note that R_0 must be determined *a priori* to the determination of the scattering angle[25]

$$1 - b^2/R_0^2 - V(R_0)/E_T = 0. \quad (4)$$

Equation (4) is nonlinear, and the application of the Newton–Raphson scheme[2] can yield the solution when b, E_T, and $V(R)$ are known. It is impossible to solve Eq. (3) by direct numerical integration since the denominator tends to zero in the limit $R = R_0$. For this reason, the Gauss–Mehler formula[14] is used to solve Eq. (3).

In most cases, the Morse potential given in Eq. (2) can be employed to simulate Xe^+–Xe collisions. Nevertheless, its maximum value, V_{max}, is 3273.77 eV at $R = 0$, which is not suitable for the elastic collision with higher energy. Furthermore, when $b = 0$, there exists no solution to Eq. (3) for $E_T > V_{max}$. For example, the variation in θ_{CM} as a function of b computed by the Morse potential in the laboratory (lab) frame at $E/q = 7{,}000$ eV is shown in Fig. 2. E_T equals half E/q, which is larger than V_{max}. Because of the singularity, θ_{CM} is below 50° except for $b = 0$ and the curve appears at an inflection point when $b \to 0$. In the neighborhood of the inflection point, θ_{CM} decreases dramatically and then increases with increasing impact parameter, which is obviously unreasonable.

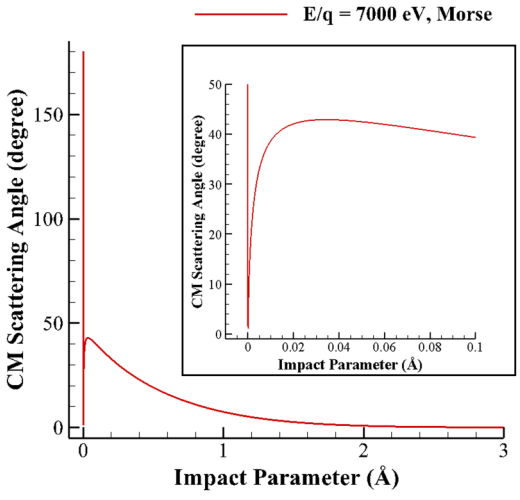

FIG. 2. Scattering angle computed by the Morse potential at $E/q = 7000$ eV.

The present study attempts to fit the spin–orbit free potentials using another form. The statistical weights of $^2\Sigma_u$, $^2\Sigma_g$, $^2\Pi_u$, and $^2\Pi_g$ potentials are 1/6, 1/6, 1/3, and 1/3, respectively.[16] An interaction potential can be obtained through weighting the four energy curves obtained by an *ab initio* method[19]

$$V_{ab\ initio} = \frac{1}{6}V_2\sum\nolimits_u + \frac{1}{6}V_2\sum\nolimits_g + \frac{1}{3}V_2\prod\nolimits_u + \frac{1}{3}V_2\prod\nolimits_g. \quad (5)$$

This "*ab initio*" potential, $V_{ab\ initio}$, gives a repulsive force that is stronger than the $^2\Sigma_u$ and $^2\Pi_g$ potentials. Additionally, the effect of Xe^+–Xe interactions is strongly repulsive at short distances but weakly attractive at larger distances.

In Ref. 26, an exponential repulsive potential is employed to simulate the interactions between atoms and ions. The repulsion energy mainly arises from the Pauli Exclusion Principle, and the potential can be calculated by the atomic distortion and the combining rule. In general, the repulsive force increases sharply, and the potential energy approaches infinity as $R \to 0$. However, the exponential potential gives a finite value at $R = 0$, the same as in the Morse potential. Accordingly, the present study attempts to modify the exponential repulsive potential. The improved potential model should be consistent with Eq. (5) and has an infinite value at $R = 0$. In Ref. 23, an exponential function was used to fit the $^2\Sigma_g$ and $^2\Pi_u$ potentials. By adjusting the model parameters, an original modified model, $V_{original}$, (6) can fit the "*ab initio*" potential (5) at large internuclear distances,

$$V_{original}(R) = (c_1 + c_2/R)e^{-c_3R}, \quad (6)$$

where c_1, c_2, and c_3 are listed in Table II.

The "*ab initio*" potential (5), the Morse potential (2), and potential (6) are compared as shown in Fig. 3, which shows that all the results are practically identical. The curves near the potential well are shown in Fig. 3(b). The maximum difference among the three potentials at the potential well is no more than 0.02 eV; therefore, the original modified potential curve in the low-lying state is in good agreement with that of the "*ab initio*" potential.

B. Modified screened-Coulomb potential

In fact, the electric overlap in the interacting atomic systems is significant at short distances, whereas that overlap can be neglected at large distances.[47] Therefore, the simulated potentials employing the data at both short and large distances are presented in this work.

Equation (6), indeed, is similar to the Buckingham function as follows:[40]

$$V(R) = \frac{Z_A Z_B}{R}(1 + p_1R + p_2R^2 + p_3R^3 + \cdots)e^{-\lambda R}, \quad (7)$$

TABLE II. Original modified potential parameters (in atomic units).

c_1	c_2	c_3
−20.7947	134.6279	0.8349

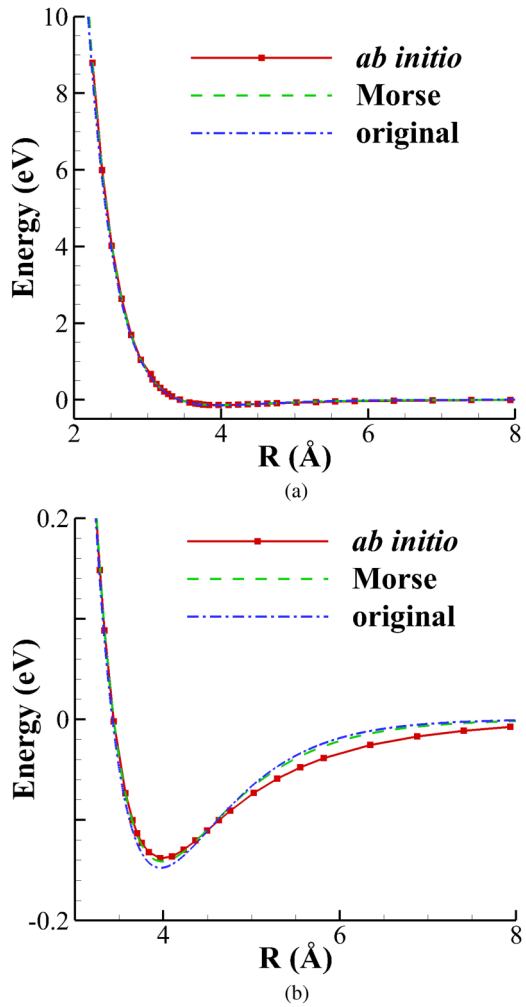

FIG. 3. Comparisons of the "*ab initio*" potential, Morse potential, and original modified potential (a) at large distances and (b) at the potential well.

where Z_A and Z_B are the atomic numbers of A and B, respectively; p_1, p_2, p_3, and λ denote model parameters in atomic units. The polynomial in Eq. (7) is used to give the correct initial behavior, a better way of interpreting the experimental results and a validity extending to larger distances.[43] In fact, Eq. (7) is one of the screened-Coulomb potentials[13]

$$V(R) = \frac{Z_A Z_B}{R} f(R), \tag{8}$$

where $f(R)$ is a screening function. When $R \to 0$, $f(R)$ approaches to one since the electron screening becomes negligible.[46] Accordingly, potential (6) can be rewritten as follows:

$$V_{original}(R) = \frac{Z^2}{R}\left(a_0 + a_1 \frac{R}{a_f}\right) e^{-\beta \frac{R}{a_f}}, \tag{9}$$

where $Z = 54$ for xenon, $a_0 = 4.617 \times 10^{-2}$, $a_1 = -1.053 \times 10^{-3}$, $\beta = 1.232 \times 10^{-1}$, and a_f is the screening length given by Firsov[41] (all the above model parameters are in atomic units),

$$a_f = 0.8853(Z^{0.5} + Z^{0.5})^{-2/3}. \tag{10}$$

Obviously, $V_{original}$ is not a screened-Coulomb potential since $a_0 \neq 1$. Equation (9) is reduced by a factor of 4.617×10^{-2} compared with a screened-Coulomb potential. The results imply that a_0 is not a constant if the screened-Coulomb type potential is still intended to be employed in this study.

The "*ab initio*" potential obtained in Ref. 19 and the potential derived from experimental scattering data[42] are used to recalibrate a_0 in Eq. (9) when it is assumed that a_1 and β are fixed. Accordingly, as shown in Fig. 4, the relationship between a_0 and R can be calculated through Eq. (9). The curve obtained by Refs. 19 and 42 implies that a_0 is an exponential decay function depending on R at short distances. Note that the decreasing at $R > 9$ has little impact on Eq. (9) since the interaction potential attenuates to zero very quickly in this domain.

The effective potential can be obtained through fitting the curve of $a_0(R)$. Equation (9) becomes as follows:

$$V_{modified}(R) = \frac{Z^2}{R}\left(q_1 + q_2 e^{-\gamma R/a_f} + a_1 \frac{R}{a_f}\right) e^{-\beta \frac{R}{a_f}}, \tag{11}$$

where q_1, q_2, and γ are the model parameters in atomic units. In the present study, two groups of parameters are employed to fit $a_0(R)$ derived from experimental scattering data.[42] For simplicity, the two potential curves are called M1 and M2, which correspond to their respective parameters.

M1 is a screened-Coulomb potential, which requires $q_1 + q_2 = 1$, while M2 is obtained by directly fitting $a_0(R)$ without the limitations of q_1 and q_2. The ratio of M2 to the screened-Coulomb

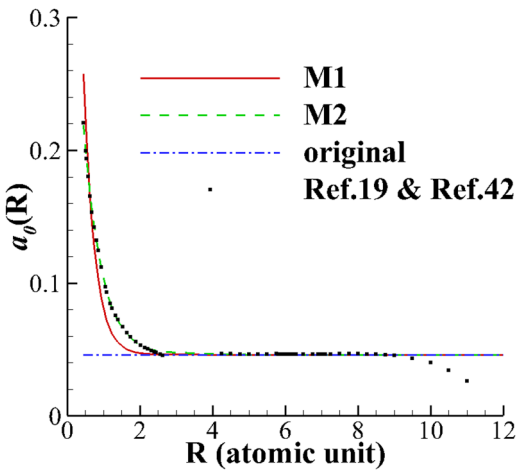

FIG. 4 Function $a_0(R)$ and the fitting curves using M1, M2, and the original modified potentials.

TABLE III. Model parameters for M1 and M2. Values are given in atomic units.

Potential	q_1	q_2	γ
M1	0.046 17	0.953 83	0.492 10
M2	0.046 17	0.431 91	0.299 83

potential is 0.478 when $R \to 0$. The parameters of the two potential curves are listed in Table III. In Fig. 4, the comparisons of functions $a_0(R)$ obtained by potential (6), M1, and M2 are made with the one calculated by Refs. 19 and 42. Results indicate that M2 is the best one.

To compare with the two fitting curves, in the present study, two screened-Coulomb potentials, ZBL and Zinoviev potential, are applied,[38,39]

$$V_{ZBL}(R) = \frac{Z^2}{R}(0.1818e^{-3.2R/a_u} + 0.5099e^{-0.9423R/a_u} + 0.2802e^{-0.4029R/a_u} + 0.02817e^{-0.2016R/a_u}), \quad (12)$$

$$V_{Zinoviev}(R) = \frac{Z^2}{R}e^{-\frac{R/a_f}{0.47+0.705(R/a_f)^{1/2}-0.025R/a_f}}, \quad (13)$$

where a_u is the screening length given by Ref. 38,

$$a_u = 0.8853(Z^{0.23} + Z^{0.23}). \quad (14)$$

In Eqs. (12)–(14), the parameters are in atomic units.

The Xe^+–Xe interaction potentials computed by M1, M2, the Morse, ZBL, and Zinoviev potential are compared with the potential derived from the experimental scattering data[42] and that obtained by an *ab initio* method[19] as depicted in Fig. 5. All of the interaction potentials are in good agreement with the data in Ref. 42 at short distances, except for the Morse one, which gives a considerable low prediction. At large distances, M1, M2, and the Morse potential match well with the data in Ref. 19, while the ZBL and Zinoviev potential give a poor prediction. The unsatisfactory results are significant at the potential well since the ZBL and Zinoviev potential ignore the attractive behavior, as plotted in Fig. 5(b).

The relative error compared with the potential derived from the experimental scattering data[42] at 0.2 Å < R < 1.4 Å for different potentials can be estimated using the formula

$$\delta V = \left|\frac{V_{\text{int}}(R) - V_{\text{exp}}(R)}{V_{\text{exp}}(R)}\right|, \quad (15)$$

where V_{int} represents the corresponding interaction potential (M1, M2, the ZBL, and Zinoviev potential) and V_{exp} represents the potential derived from experimental scattering data,[42] respectively. As plotted in Fig. 6, the relative error for each potential is no more than 30% at short distances. Compared with M1 and ZBL potentials, M2 and Zinoviev potentials are better with the potential derived from experimental scattering data.[42]

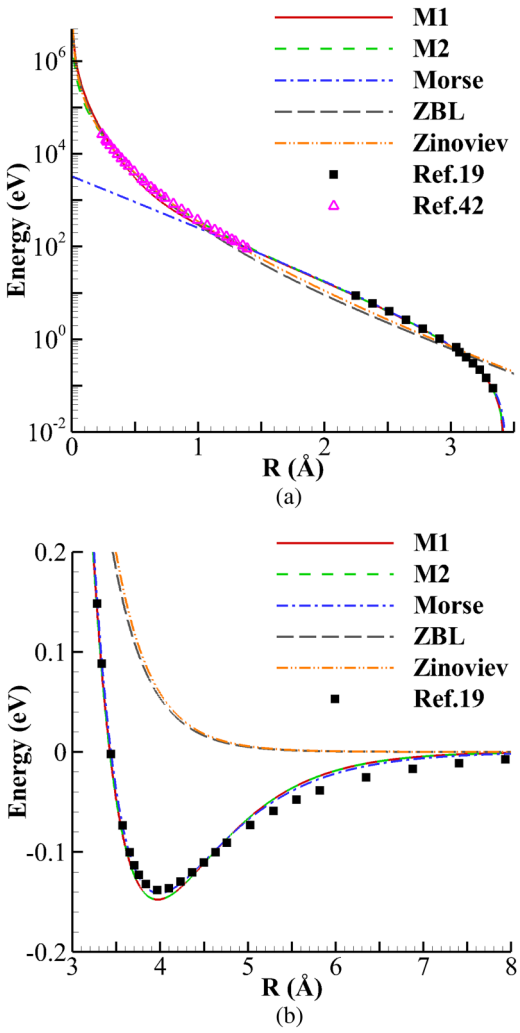

FIG. 5 The interaction potentials for Xe^+–Xe calculated by different potentials (a) at short distances and (b) at the potential well.

C. Collision dynamics

Considering that M1 and M2 have been obtained through spin–orbit free interaction potentials and the screened-Coulomb potential, the next step is to validate the features of the model.

Figures 7 depict the CM scattering angle, θ_{CM}, computed using M1, M2, the Morse, ZBL, and Zinoviev potential in the lab frame at $E/q = 5$, 300, 1,500, and 7000 eV. The curves become steeper as the energy increases, while the scattering angles attenuate to zero more quickly, indicating that the cross section decreases correspondingly.

In Figs. 7(a) and 7(b), the scattering angles calculated by M1 and M2 are essentially the same as those obtained by the Morse potential. The ZBL and Zinoviev potential cannot obtain a negative θ_{CM} in low-energy regions since they completely ignore the attractive behavior. At $E/q = 1500$ eV, the scattering angles obtained by M1

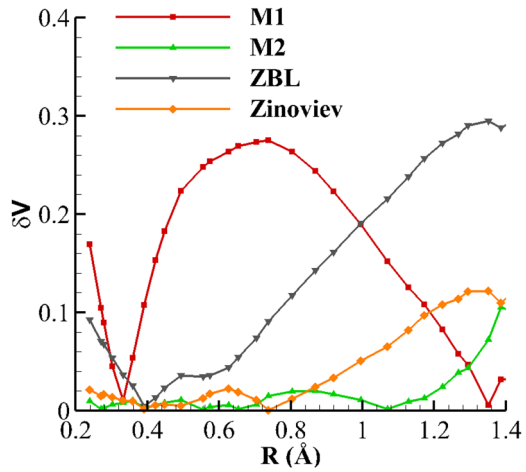

FIG. 6 The relative error for M1, M2, ZBL, and Zinoviev potentials at short distances.

and M2 match better with the results obtained by the ZBL and Zinoviev potential, indicating that the repulsive effect becomes significant. In small impact-parameter region, the scattering angle calculated by the Morse potential is considerably smaller than that calculated by other four potentials due to its weaker repulsive effect.

The curve obtained by the Morse potential at $E/q = 7000$ eV is obviously unreasonable due to the singularity when the impact parameter approaches to zero, which has been analyzed in Sec. II A. On the other hand, the results obtained by M1 and M2 conform with those obtained by the ZBL and Zinoviev potential.

The above discussion indicates that the model can give a good prediction on the scattering angles both in low and high energy regions.

The differential cross section in the CM frame can be used to further verify the effective potential, which is defined as follows:[29]

$$d\sigma(\theta_{\mathrm{CM}}, E_T)/d\Omega_{\mathrm{CM}} = \left|\frac{b}{\sin\theta_{\mathrm{CM}}} \cdot \frac{db}{d\theta_{\mathrm{CM}}}\right|. \tag{16}$$

The probability distribution of the scattering angle can be evaluated using the relation between the differential cross sections

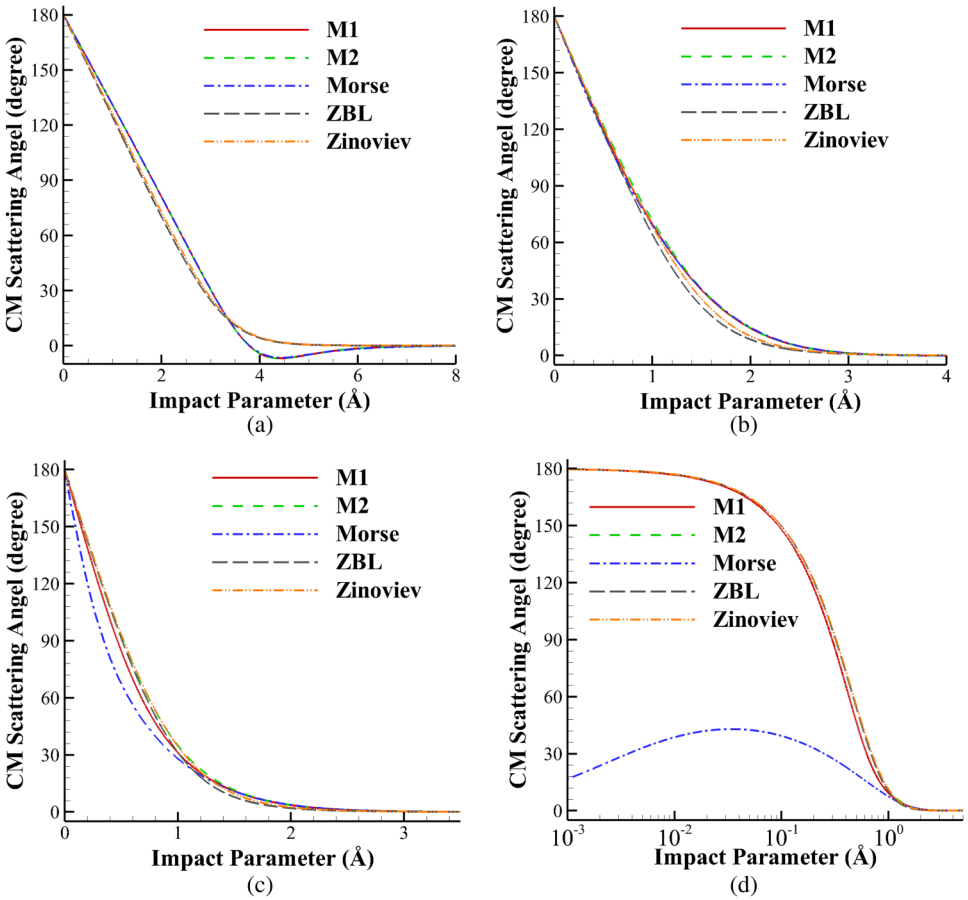

FIG. 7 Scattering angles computed by different potentials at (a) $E/q = 5$ eV, (b) $E/q = 300$ eV, (c) $E/q = 1500$ eV, and (d) $E/q = 7000$ eV.

and the scattering angles. Thus, the postcollision velocities of the particles are obtained accordingly.[15,17,18,28]

For the CEX collision, a weighted averaging method is employed to calculate the differential cross section. Accordingly, expression (16) can be rewritten as follows:[16]

$$d\sigma(\theta_{\rm CM}, E_T)/d\Omega_{\rm CM} = [1 - P_{CEX}(\theta_{\rm CM})]\frac{d\sigma(\theta_{\rm CM})}{d\Omega_{\rm CM}} + P_{CEX}(\theta_{\rm CM})\frac{d\sigma(\pi - \theta_{\rm CM})}{d\Omega_{\rm CM}}, \quad (17)$$

where $P_{CEX}(\theta_{CM})$ is the angle-dependent CEX probability. Considering that P_{CEX} oscillates rapidly between 0 and 1, an average value of 0.5 is used in this study for simplicity.[16,17,28] Obviously, the differential cross section can be obtained if the function between the scattering angle and the impact parameter is determined.

Figures 8 plot the differential cross sections calculated by M1, M2, the Morse, ZBL, and Zinoviev potentials as functions of CM scattering angles for ion energies in the lab frame at $E/q = 5$, 300, 1500, and 7000 eV, respectively. The calculations are performed for inclusion of CEX collisions. The peaks of the differential cross sections appear at 0° and 180°, indicating that the MEX collisions mainly take place in the region of relatively small scattering angles and the CEX collisions mostly take place at large scattering angles.

The differential cross sections calculated by the Morse potential are significantly different from those calculated by the ZBL and Zinoviev potentials due to their different deflection functions. At $E/q = 5$ eV and 300 eV, the results obtained by M1 and M2 are in good agreement with those obtained by the Morse potential. While in higher energy region, results calculated using M1 and M2 match well with those calculated using the ZBL and Zinoviev potential. In particular, the curves of differential cross sections calculated by the Morse potential are incomplete and even "curl" at $E/q = 7000$ eV since this potential cannot exhibit any scattering at angles greater than 50° and the deflection function becomes non-monotonic.

A functional form of the Xe^+–Xe CEX cross section is expressed as[27]

$$\sigma_{CEX} = 87.3 - 13.6\log(E_{lab})\ \text{Å}^2, \quad (18)$$

where E_{lab} (eV) is the energy of Xe^+ in the lab frame. Here, the energy of Xe is negligible, since it is at least two orders of magnitude lower than that of Xe^+. For sufficiently large internuclear distance, the interaction effects between the ion and atom tend to be

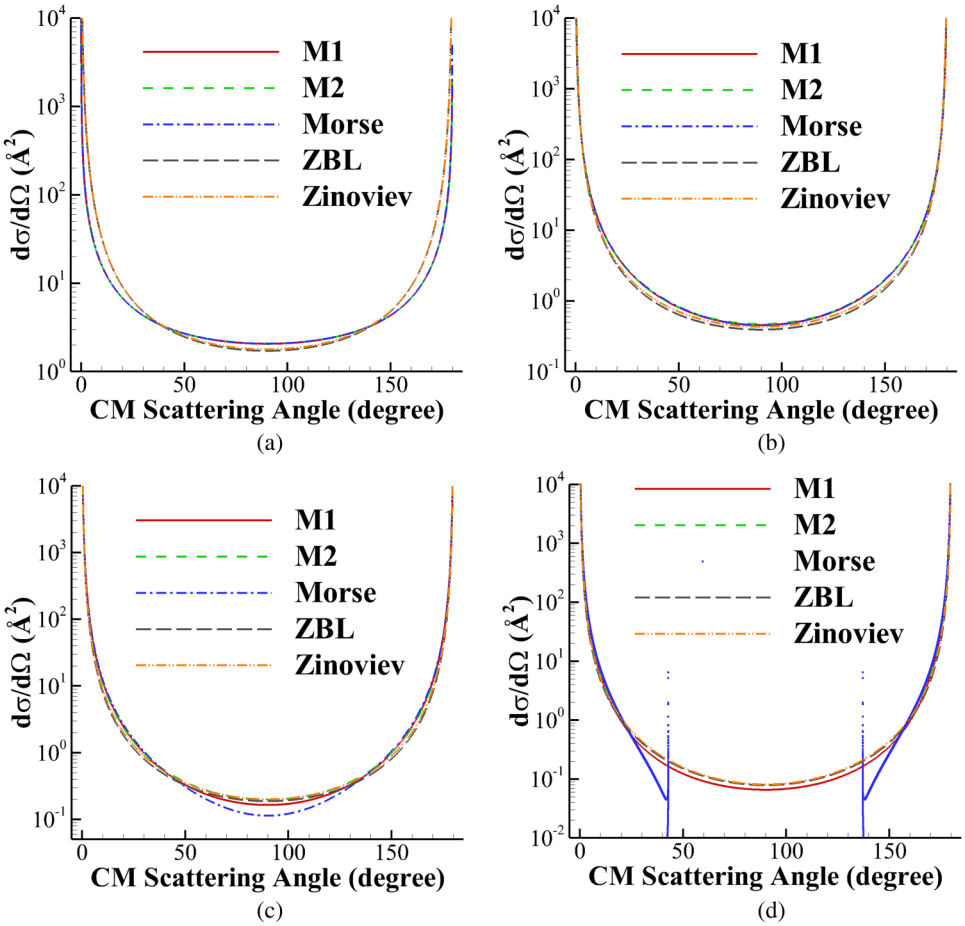

FIG. 8. Absolute elastic scattering differential cross sections calculated using different potentials with CEX collisions at (a) $E/q = 5$ eV, (b) $E/q = 300$ eV, (c) $E/q = 1500$ eV, and (d) $E/q = 7000$ eV.

extremely weak, and the scattering angle tends to zero. It is necessary, however, to cut off the impact parameter during numerical integration. Thus, the impact cross section of the particles can be regarded as a circle whose radius is the cut-off impact parameter, namely, $\sigma = \pi b^2$.

In addition, since an average CEX probability of 0.5 is assumed,[16,17,28] the total cross section, σ_{totab} should be twice the CEX cross section, i.e., $\sigma_{total} = 2\sigma_{CEX}$. The maximum impact parameter, b_{max}, can be obtained through the formula: $\sigma_{total} = \pi b_{max}^2$. The CM scattering angles calculated by M1, M2, the Morse, ZBL, and Zinoviev potentials at the maximum impact parameter are always less than 1° in the energy range of this study.

III. NUMERICAL PROCEDURES

To validate the effective potential, a benchmark problem based on the experiment conducted by Patino,[22]—in which a collimated 1500-eV, single-charged xenon ion beam is injected into a test cell, colliding with the xenon target gas—is simulated using the PIC-MCC technique in conjunction with a direct method for solving the scattering equation. Accordingly, the injection of 7000 eV xenon ions into the test cell is simulated to make the comparisons among different potentials at higher energy.

Because this study focuses on Xe^+–Xe elastic collisions, wall–ion interactions and secondary electron emission are neglected. Additionally, the present study uses different interaction potentials to simulate Xe^+–Xe elastic scattering without changing any other setup. Therefore, the evaluation of these potentials seems unaffected by ignoring wall–ion interactions and secondary electron emission.

A. Physical model

The test cell is an experimental facility, which has been used in a series of studies[17,18,21,22,30–32,48,49] for providing detailed data of the interactions between injected ions and background atoms. The setup is designed as a cylinder to provide a simple axisymmetric numerical domain. In the test cell, the experimental and computed currents are collected on the inner cylinder (IC), exit plate (EP), exit orifice (EO), and front plate (FP) electrode to investigate collisions between the ions and atoms. Moreover, the single inner cylinder is replaced with three cylindrical electrodes (IC1, IC2, and IC3) for a more detailed analysis of the ionic-atomic scattering properties along the inner cylinder.

As presented in Fig. 9, the computational domain is a two-dimensional axisymmetric cylinder, 41.2 mm in diameter and 160 mm long, in which IC1 = 50 mm, IC2 = 50 mm, and IC3 = 60 mm. The inflow and exit orifices are set coaxially with diameters of 3.2 mm and 5 mm, respectively.

B. PIC-MCC method

The particle-in-cell (PIC) technique is a particle simulation technique[33] which tracks the motion of charged macroparticles. In this study, each macroparticle is regarded as a collection of real ions. The computational domain is divided into cells in order to save the field information onto the nodes, such as plasma potential, electric field, and number density of ions. Figure 10 presents the computational grids for the simulation. The number of cells is about 3500, and the maximum length of the cell is smaller than the Debye length.

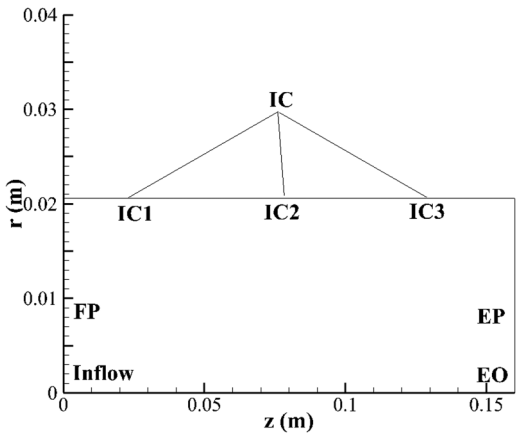

FIG. 9. Two-dimensional axisymmetric computational domain of the test cell.

The mesh is a nonuniform rectangle, therefore, the weighting scheme developed by Ruyten[34] can be employed to ensure the conservation of charge density. The weight of a macroparticle is set to 25, meaning that a macroparticle represents 25 xenon ions. With increasing background pressure, the number of macroparticles in the computational domain changes from about 4×10^4 to 5×10^5 at a steady state.

Because the charged particles consist of only xenon ions in the test cell, the potential can be obtained by solving Poisson's equation if the effect of self-consistent magnetic fields is neglected. In one time-step cycle of the PIC method, the electric field is calculated by differentiating the plasma potential. Subsequently, the velocities of the macroparticles are updated using the present electric field. Finally, these macroparticles are moved using the updated velocities.

A time step of 6.53×10^{-8} s is employed in the simulation to assure that it is smaller than the inverse of the plasma oscillation

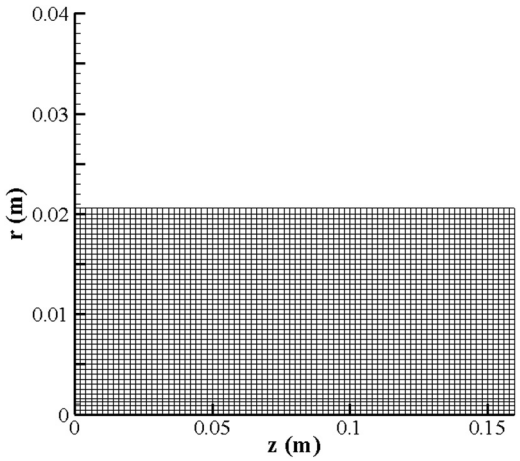

FIG. 10. Computational grids for the simulation of the test cell.

frequency. The simulations take 1.2×10^4 time steps to reach a steady state. Additionally, in order to eliminate noise, another 4×10^3 time steps are required for sampling.

A Monte Carlo collision (MCC) method is used to simulate the collisions of charged particles with neutral atoms.[20] In this study, because the number densities of xenon ions are $10^{10}\,m^{-3}$ and those of xenon atoms are changing from $10^{17}\,m^{-3}$ to $10^{20}\,m^{-3}$, it can be assumed that ion-neutral collisions have little effect on the atoms. The probability that a macroparticle experiences an elastic collision in a time step is given by

$$P = 1 - \exp(-v_i n_0 \sigma_{total} \Delta t), \tag{19}$$

where Δt is the time step, v_i is the velocity of Xe^+, n_0 is the number density of xenon atoms, and σ_{total} includes both the MEX and CEX cross sections. When simulating a collision, the first step is to determine whether the collision occurs. If P is larger than a random number between 0 and 1, an assumption is made that elastic scattering occurs, and then the next step involves determining whether the collision type is MEX or CEX. Additionally, in the case of a CEX collision, the postcollision velocities are required to be switched between Xe^+ and Xe.

C. A direct method solving the scattering equation

With increasing background pressure in the test cell, the number density of xenon atoms increases, resulting in more collisions between xenon ions and xenon atoms. The average collision frequency of Xe^+ in the facility changes from less than one to greater than one. In general, this type of collision reduces ion energy and gives rise to the various values of resulting energy. Accordingly, the method using the relationship between the scattering angle and the differential cross section, for a specific energy, to determine the scattering angle is inexact.[15]

For this reason, a direct method solving the scattering equation is employed in the present study, which is compatible to a wide range of ion energies and thus provides more reliable scattering properties.

D. Boundary conditions

The present simulation only tracks the motion of ions. The xenon ions are injected into the test cell from the inflow. Ions that do not collide mostly exit from the exit orifice, while other ions experiencing collisions collide with the walls (FP, IC, and EP). It is assumed that any ions colliding with the walls are neutralized and then exit

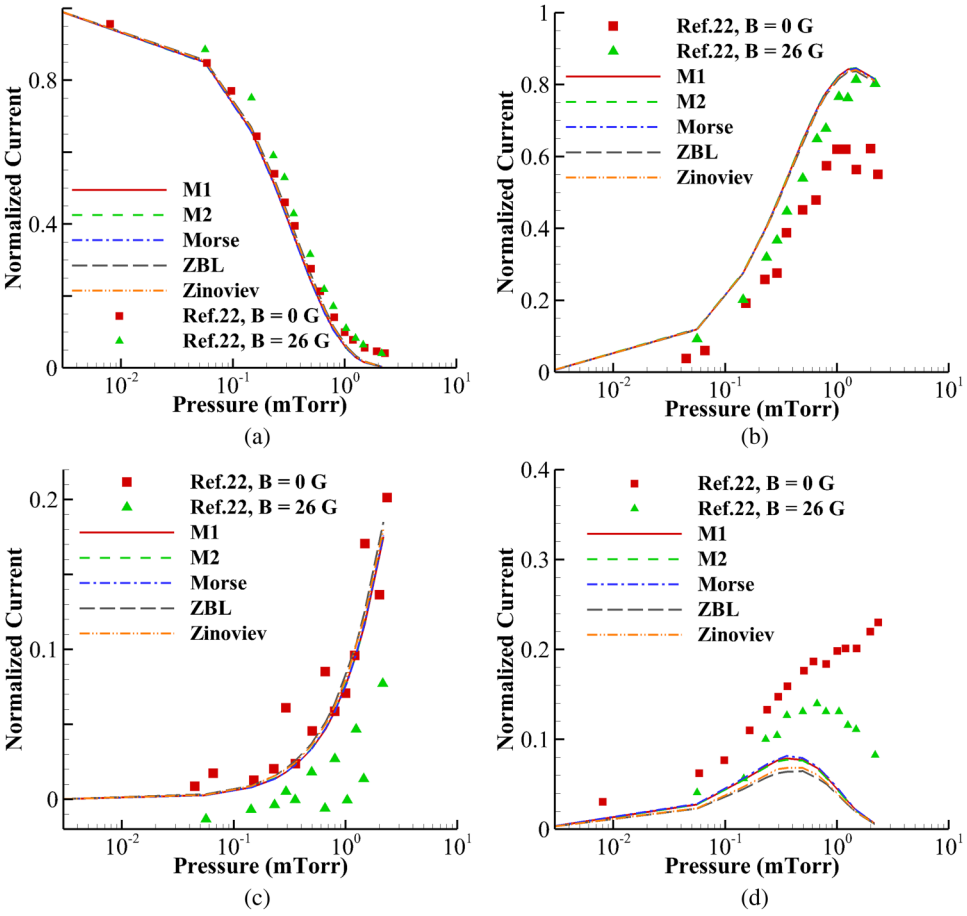

FIG. 11. Comparisons of normalized currents on (a) EO, (b) IC, (c) FP, and (d) EP between experiments and simulated results via different potentials at E/q = 1500 eV.

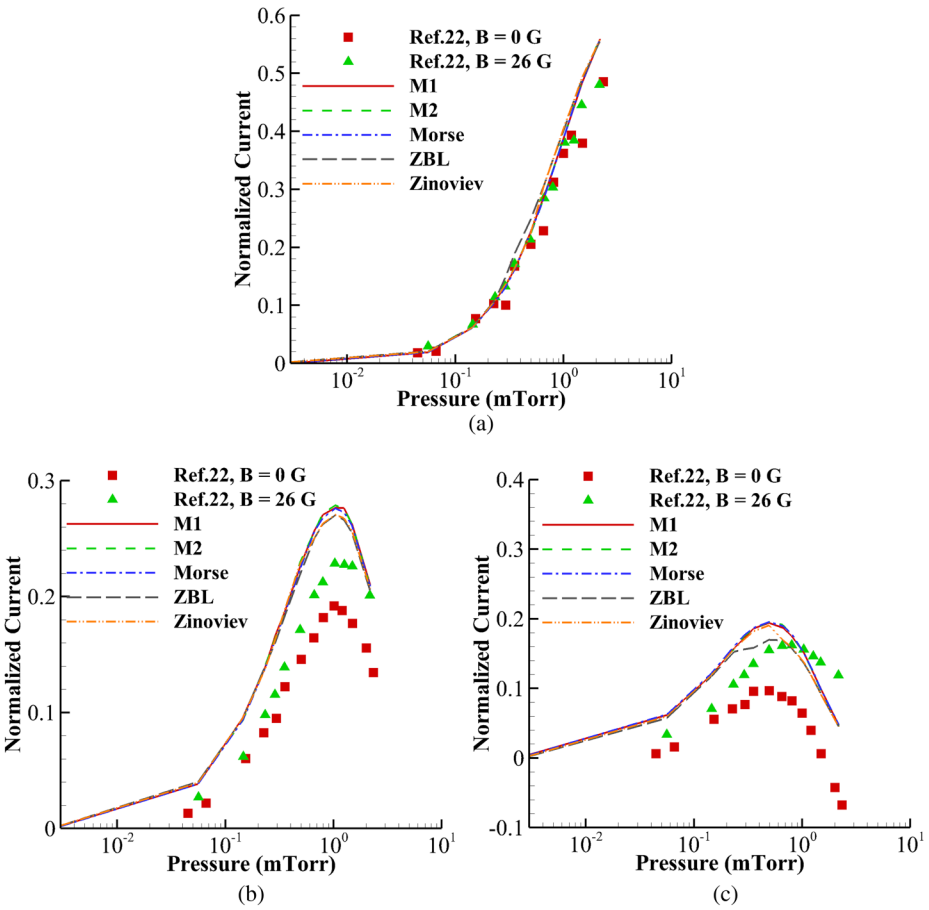

FIG. 12. Comparisons of normalized currents on (a) IC1, (b) IC2, and (c) IC3 between experiments and simulated results via different potentials at $E/q = 1500$ eV.

the computational domain. In addition, a specular reflection occurs when a macroparticle passes through the symmetry axis.

The current injected into the test cell in the benchmark problem is assumed to be 17.727 nA, with a uniform velocity profile in the plane normal to current direction. The velocity of Xe^+ at 1500 eV is 4.69×10^4 m/s. The temperature of the background xenon atoms under consideration is 300 K, and the density distribution of atoms in the test cell is uniform. The setups in the $E/q = 7000$ eV case are the same as those in the benchmark except for the faster initial ion velocities.

The plasma potential at the boundary surfaces must be specified. In this study, a Dirichlet condition is employed on the wall and in the inflow, where the potential is set to zero. A Neumann condition is used in the exit orifice and symmetry axis, meaning that the potential gradient normal to the boundary edges is zero.

IV. RESULTS AND DISCUSSION

A. Simulation at $E/q = 1500$ eV

1. Currents on EO, FP, IC, and EP

Figure 11 presents the comparisons of simulated currents for M1, M2, the Morse, ZBL, and Zinoviev potentials collected on EO, FP, IC, and EP using experimental measurements. All currents are normalized by the total currents entering the test cell,

$$\overline{I_j} = I_j/(I_{FP} + I_{IC} + I_{EP} + I_{EO}), \tag{20}$$

where j represents the given electrode (FP, IC, EP, or EO). The experiment[22] includes one group in the absence of a magnetic field and the other with an axial magnetic field of 26 G. The magnetic field confines electrons within quite a small gyroradius, without restricting ions. Since electrons can be produced by atomic ionization or particle-induced electron emission at high pressure, the axial magnetic field ensures that the currents on IC are mostly composed of ions.

In Fig. 11(a), the simulated currents for different potentials are identical and conform with the experimental data. The currents through the exit orifice decrease from 1 to 0 as pressure increases. In fact, the collision probability of Xe^+–Xe increases with the number density of xenon atoms, and ions experiencing large-angle scattering are mainly collected on FP, IC, and EP. Correspondingly, the currents through EO decrease, and the experimental results collected on EO are independent of the magnetic field, implying that almost no electrons exit through EO.

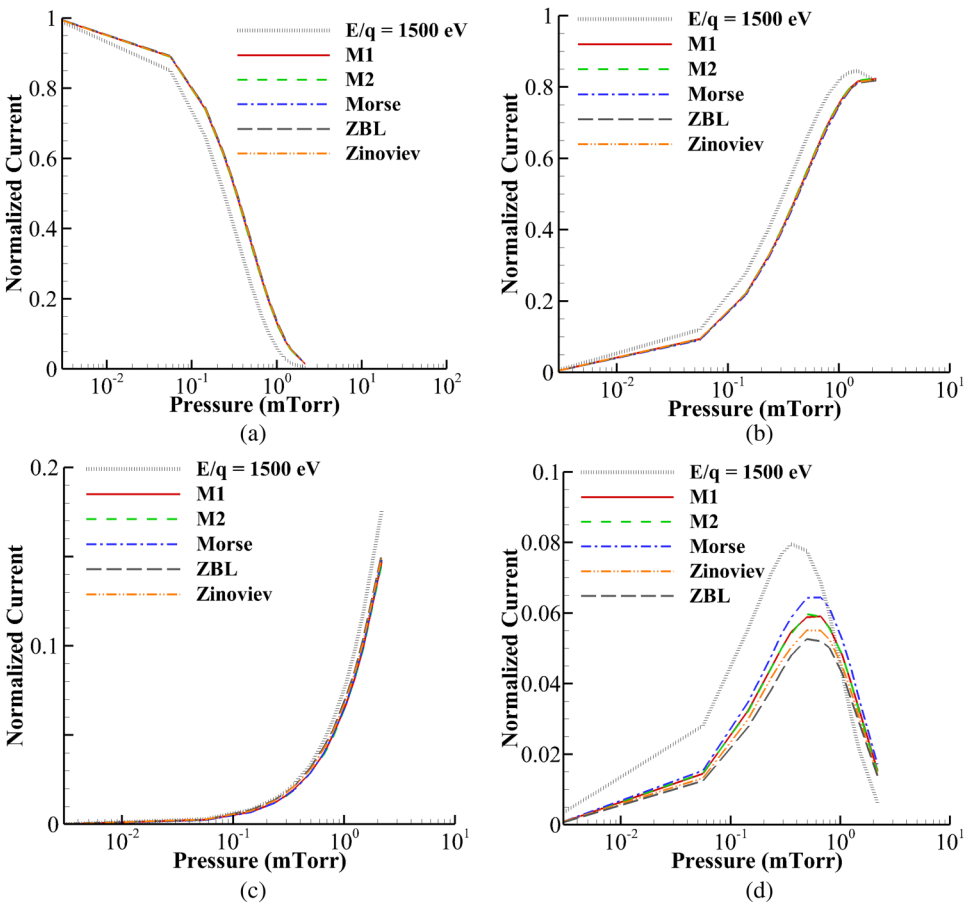

FIG. 13. Comparisons of normalized currents on (a) EO, (b) IC, (c) FP, and (d) EP between the simulated results via the Morse potential at $E/q = 1500$ eV and those via different potentials at $E/q = 7000$ eV.

Figure 11(b) shows that the currents are collected on IC rapidly and then decrease slowly with increasing pressure. The currents for different potentials still match well. At high pressure, the ions experiencing several collisions can trigger large-angle scattering and collide with FP, resulting in a reduction in the currents collected on IC. In addition, more electrons are generated at higher pressure. Since the axial magnetic field prevents electrons from colliding with IC, the experimental currents collected on IC with a magnetic field are larger than those without a magnetic field. Considering that the present simulation neglects electrons, the computed currents better match the experimental results with a magnetic field.

Figure 11(c) plots the currents collected on FP, increasing with increasing pressure. Since an axial magnetic field repels the electrons from IC, the electrons must be collected on FP or EP. In the case without a magnetic field, they are expected to scatter isotropically and collide with any wall in the facility. Accordingly, the experimental currents collected on FP in the absence of a magnetic field are larger than those in the presence of an axial magnetic field. This means that the effect of electrons on FP without a magnetic field is weaker than the effect in the presence of a magnetic field. Accordingly, the simulated results are in better agreement with the experimental currents without a magnetic field. The currents via the ZBL and Zinoviev potential are slightly larger than those via other three potentials, mainly due to the larger scattering angles computed by the former two screened-Coulomb potentials at small impact-parameters.

Figure 11(d) depicts the currents collected on EP. The electrons can be generated from EP at high pressure. When no magnetic field is exerted, they are likely to collide with IC, indirectly causing an increase in positive current collected on EP. Therefore, the experimental current continually increases with increasing pressure. However, at high pressure, there is a decrease in current in the presence of an axial magnetic field, since the emitted electrons are likely to accumulate on FP and EP, and thus partly offset the loss of electrons on EP. Because of the neglect of electrons in the present simulation, the computed currents collected on EP better match the measurements taken in the presence of an axial magnetic field. The ZBL and Zinoviev potential underestimate the currents on EP mainly because those two potentials predict the larger scattering angle at small impact-parameter region compared with other three potentials.

2. Currents on IC1, IC2, and IC3

Figure 12 plots the comparisons between the computed normalized currents via different potentials and the experimental results

collected on IC1, IC2, and IC3. The results from M1, M2, and the Morse potential almost coincide, but they are different from the currents from the ZBL and Zinoviev potential at high pressure.

In Fig. 12(a), the computed currents match well with those from the experiments collected on IC1, in which the current increases with increasing pressure. The continual increase in currents is mainly due to more ions experiencing large-angle scattering. The magnetic field has almost no effect on the currents in this region, implying that the emitted electrons are unlikely to collect on the upstream of the inner cylinder (IC1). The currents from the ZBL and Zinoviev potential are slightly larger than those from other three potentials, since there are more large-angle scattered MEX ions calculated by the former two screened-Coulomb potentials.

Figure 12(b) shows the currents collected on IC2. The computed currents and the experimental currents first increase as pressure increases and then decrease at high pressure. There are two reasons for decreasing currents at high pressure. One is that the ions which experience several collisions are likely to collect on the upstream of the test cell; the other is that the emitted electrons are expected to collect on IC2. The experimental currents in the presence of an axial magnetic field are larger than those in the absence of a magnetic field, since the field can prevent electrons from collecting on IC. The currents computed by the ZBL and Zinoviev potential are slightly smaller than those obtained by other three potentials at high pressure. Compared with the other three potentials, results from the two screened-Coulomb potentials are in better agreement with the experimental data. However, it happens that the result can take place since the currents computed by these two purely repulsive models are more likely to be collected on IC1 and FP.

As seen in Fig. 12(c), the variation in currents collected on IC3 is similar to the variation in currents on IC2. However, the experimental currents in the absence of a magnetic field are negative at high pressure, implying that IC3 collects more electrons than ions. For the reason given in the previous paragraph, the computed results from the ZBL and Zinoviev potential are smaller than those computed from the other three models at high pressure.

B. Simulation at $E/q = 7000$ eV

1. Currents on EO, FP, IC, and EP

The normalized currents obtained by M1, M2, the Morse, ZBL, and Zinoviev potentials at $E/q = 7000$ eV and those computed using

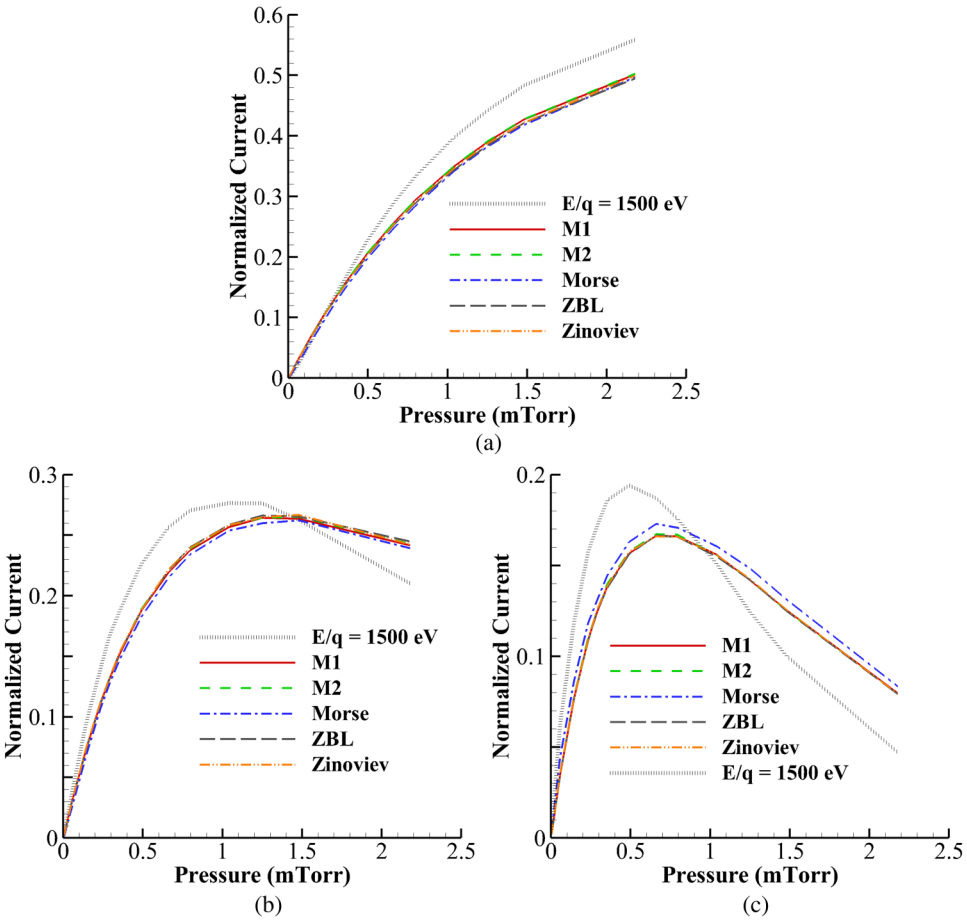

FIG. 14. Comparisons of normalized currents on (a) IC1, (b) IC2, and (c) IC3 between the simulated results via the Morse potential at $E/q = 1500$ eV and those via different potentials at $E/q = 7000$ eV.

the Morse one at $E/q = 1500$ eV are shown in Figs. 13. Results show that the currents via these five models at $E/q = 7000$ eV are identical on EO and IC, but those currents on FP and EP are different.

Because of the increase in the velocities, the collision cross sections are reduced, and the mean free path is increased; therefore, at high energy, more ions that have not collided exit the test cell from EO. For the same reason, the currents on IC and FP at $E/q = 7000$ eV are larger than those at $E/q = 1500$ eV, as plotted in Figs. 13(b) and 13(c), respectively. As shown in Fig. 13(d), at low pressure, the currents on EP show a similar tendency to the currents on IC and FP; however, with increasing pressure, the currents at $E/q = 7000$ eV are larger than those at $E/q = 1500$ eV.

From Fig. 7, it can be seen that the scattering angle decreases with increasing energy in the large-angle scattering region. Most of the ions have experienced multiple collisions at high pressure. Therefore, the ions at $E/q = 7000$ eV are more likely to collide on EP due to smaller-angle scattering, while the ions at $E/q = 1500$ eV probably collide on IC or FP due to the superposition of the larger-angle scattering.

At $E/q = 7000$ eV, the simulated currents on EP from the Morse potential are the largest; those via M1 and M2 are practically identical; and those computed through the ZBL and Zinoviev potentials are smaller than other three results. Accordingly, it can be seen that the Morse potential underestimates the large-angle scattered ions due to the absence of a scattering angle above 50°. The ZBL and Zinoviev potentials, however, predict more large-angle scattered ions since they ignore the attractive effect. Those results imply that the model proposed in this study is more reasonable.

2. Currents on IC1, IC2, and IC3

To further verify the disparities among different potentials, normalized currents on IC1, IC2, and IC3 computed using the Morse potential at $E/q = 1500$ eV and those using different potentials at $E/q = 7000$ eV are presented in Fig. 14.

In Fig. 14(a), the currents collected on IC1 at $E/q = 1500$ eV are larger than those at $E/q = 7000$ eV due to the smaller scattering angle at higher energy. All the simulated results at $E/q = 7000$ eV almost coincide except for those obtained by the Morse potential which slightly underestimates the currents. This disparity is mainly because the Morse potential cannot give a scattering angle above 50°.

In Figs. 14(b) and 14(c), at high pressure, the currents at $E/q = 1500$ eV are smaller than those at $E/q = 7000$ eV, since the collision frequency is increased with the increasing pressure and more ions are likely to be collected on IC1 or FP. At $E/q = 7000$ eV, the currents from M1, M2, the ZBL, and Zinoviev potentials still match well, while the Morse potential underestimates the currents on IC2 and overestimates those on IC3. Since the Morse potential cannot predict a scattering angle above 50°, more ions are likely to be collected on the downstream of the test cell (IC3 and EP).

V. CONCLUSIONS

An effective Xe^+–Xe interaction potential has been proposed based on both spin–orbit free interaction potentials and the screened-Coulomb potential. In this work, two potential curves based on the model are given: one is a screened-Coulomb type potential and the other is directly obtained through fitting the curve derived from experimental scattering data.[42] At large distances, the model matches well with the interaction potential based on an *ab initio* method. At short distances, the relative error is no more than 30% when compared with the potential derived from experimental scattering data[42] for either potential curves. Compared with the Morse, ZBL, and Zinoviev potentials, the effective potential can predict better scattering angles and differential cross sections both in low and high energy regions.

The model can be employed with the Monte Carlo technique to simulate the Xe^+–Xe elastic collisions in electric propulsion systems. To validate the effective potential, a PIC-MCC technique in conjunction with a direct method for solving the scattering equation is employed to simulate the collisions between 1500-eV, single-charged xenon ions and background xenon atoms in a test cell. The currents collected on different electrodes (EO, FP, IC, and EP) provide detailed data of the interactions between Xe^+ and Xe. The computed currents via the two potential curves and the Morse potential are basically the same, and they are all in good agreement with experiment. While larger currents are likely to be collected on the upstream of the test cell using the ZBL and Zinoviev potentials since those two screened-Coulomb potentials give larger scattering angles at short distances.

In order to further show the disparities of different potentials, collisions between 7000-eV Xe^+ and Xe in the test cell are simulated. Results from the two potential curves match well with the ZBL and Zinoviev potentials. However, when compared with the other four potential curves, there are larger currents on the downstream of the test cell and lower currents on the upstream when using the Morse one. The results show that the Morse potential underestimates the large-angle scattered ions in the high energy region mainly due to the absence of a large scattering angle. Therefore, it is believed that the effective potential can provide a more reliable prediction of the elastic collisions between Xe^+ and Xe.

ACKNOWLEDGMENTS

The present work was supported by the National Key Basic Research and Development Program (2014CB744100).

REFERENCES

[1]D. M. Goebel and I. Katz, *Fundamentals of Electric Propulsion: Ion and Hall Thrusters* (Wiley, New York, 2008).
[2]R. S. Roy, "Numerical simulation of ion thruster plume backflow for spacecraft contamination assessment," Ph.D. dissertation (Massachusetts Institute of Technology, 1995).
[3]G. A. Bird, *Molecular Gas Dynamics and the Direct Simulation of Gas Flows* (Oxford University Press, Oxford, 1994).
[4]I. D. Boyd, J. Spacecr. Rockets **38**, 381 (2001).
[5]D. B. Vangilder, G. I. Font, and I. D. Boyd, J. Propul. Power **15**, 530 (1999).
[6]D. Y. Oh, "Computational modeling of expanding plasma plumes in space using a PIC-DSMC alogrithm," Ph.D. dissertation (Massachusetts Institute of Technology, 1997).
[7]T. D. Huismann and I. D. Boyd. in *32nd International Electric Propulsion Conference, Wiesbaden, Germany*, Paper No. IEPC-2011-227 (IEPC, 2011).

[8]T. D. Huismann, "Improving hall thruster plume simulation through refined characterization of near-field plasma properties," Ph.D. dissertation (University of Michigan, 2011).
[9]F. Sharipov and J. L. Strapasson, Phys. Fluids **24** 011703 (2012).
[10]P. R. Jones, G. M. Conklin, D. C. Lorents, and R. E. Olson, Phys. Rev. A **10**, 102 (1974).
[11]D. C. Lorents, R. E. Olson, and G. M. Conklin, Chem. Phys. Lett. **20**, 589 (1973).
[12]R. E. Johnson, J. Phys. Soc. Jpn **32**, 1612 (1972).
[13]I. G. Kaplan, *Intermolecular Interactions: Physical Picture, Computational Methods and Model Potentials* (John Wiley & Sons, Ltd, England, 2006).
[14]S. J. Araki, AIP Conf. Proc. **1786**, 170004 (2016).
[15]M. K. Scharfe, J. Koo, and G. Azarnia, AIP Conf. Proc. **1333**, 1085 (2011).
[16]Y. H. Chiu, R. A. Dressler, D. J. Levandier, C. Houchins, and C. Y. Ng, J. Phys. D Appl. Phys. **41**, 165503 (2008).
[17]P. N. Giuliano and I. D. Boyd, Phys. Plasmas **20**, 033505 (2013).
[18]S. J. Araki and R. E. Wirz, IEEE Trans. Plasmas Sci. **41**, 470 (2013).
[19]I. Paidarová and F. X. Gadea, J. Chem. Phys. **274**, 1 (2001).
[20]C. K. Birdsall, IEEE Trans. Plasmas Sci. **19**, 65 (1991).
[21]M. I. Patino and R. E. Wirz, Phys. Plasmas **25**, 062108 (2018).
[22]M. I. Patino, "Plasma inter-particle and particle-wall interactions," Ph.D. dissertation (University of California Los Angeles, 2017).
[23]M. Amarouche, G. Durand, and J. P. Malrieu, J. Chem. Phys. **88**, 1010 (1988).
[24]I. Katz, G. Jongeward, V. Davis, M. Mandell, I. Mikellides, R. Dressier, I. Boyd, K. Kannenberg and D. King, in *37th AIAA/ASME/SAE/ASEE Joint Propulsion Conference and Exhibit, Salt Lake City, UT*, Paper No. 2001-3355 (AIAA, 2001).
[25]M. S. Child, *Molecular Collision Theory* (Academic Press, London, 1974).
[26]F. T. Smith, Phys. Rev. A **5**, 1708 (1972).
[27]J. S. Miller, S. H. Pullins, D. J. Levandier, Y. H. Chiu, and R. A. Dressler, J. Appl. Phys. **91**, 984 (2002).
[28]I. D. Boyd and R. A. Dressler, J. Appl. Phys. **92**, 1764 (2002).
[29]W. G. Vincenti and C. H. Kruger, *Introduction to Physical Gas Dynamics* (Wiley, New York, 1963).
[30]M. Patino, L. Chu and R. Wirz, in *AIAA/ASME/SAE/ASEE Joint Propulsion Conference & Exhibit* (AIAA, 2012).
[31]P. N. Giuliano and I. D. Boyd, in *32nd International Electric Propulsion Conference, Wiesbaden, Germany* (AIAA, 2011).
[32]S. J. Araki and R. E. Wirz, in *42nd AIAA Plasmadynamics and Lasers Conference, Honolulu, Hawaii* (IEPC, 2011).
[33]C. K. Birdsall and A. B. Langdon, *Plasma Physics via Computer Simulation* (Adam Hilger, Bristol, 1991).
[34]W. M. Ruyten, J. Comput. Phys. **105**, 224 (1993).
[35]H. Yukawa, Proc. Phys. Math. Soc. Jpn. **17**, 48 (1935).
[36]J. S. Rowlinson, Physica A **156**, 15 (1989).
[37]R. K. Pathak and A. J. Thakkar, J. Chem. Phys. **87**, 2186 (1987).
[38]J. F. Ziegler, J. P. Biersack, and U. Littmark, *The Stopping and Range of Ions in Solids Vol. 1* (Pergamon, New York, 1985).
[39]A. N. Zinoviev, Nucl. Instr. Methods Phys. Res. B **269**, 829 (2011).
[40]R. A. Buckingham, Trans. Faraday Soc. **54**, 453 (1958).
[41]O. B. Firsov, Sov. Phys. Exp. Theor. Phys. **6**, 534–537 (1958).
[42]A. N. Zinoviev, Tech. Phys. **53**, 13 (2008).
[43]R. E. Duff, R. A. Buckingham, J. S. Rowlinson, A. R. Ubbelohde, E. Whalley, S. D. Hamann, K. M. Guggenheimer, A. D. Buckingham, B. Vodar, R. P. Bell, L. Galatry, H. de Kluiver, B. J. Alder, E. U. Franck, J. Jeener, M. Lambert, and L. E. Sutton, Discuss. Faraday Soc. **22**, 75–87 (1956).
[44]P. J. Wilbur and L. O. Daniels, Vacuum **36**, 5 (1986).
[45]P. J. Wilbur, AIP Conf. Proc. **361**, 155 (1996).
[46]E. Fermi, Z. Phys. **48**, 73 (1928).
[47]V. B. Leonas, Sov. Phys. Usp. **15**, 266 (1972).
[48]R. E. Wirz, L. Chu, M. Patino, H-S Mao, and S. J. Araki, in *32nd International Electric Propulsion Conference, Wiesbaden, Germany* (IEPC, 2011).
[49]S. J. Araki and R. E. Wirz, in *34th International Electric Propulsion Conference, Kobe, Japan* (IEPC, 2015).